ELSEVIER

Contents lists available at ScienceDirect

Biomaterials Advances

journal homepage: www.journals.elsevier.com/materials-science-and-engineering-c





An *in vitro* analysis of the effect of geometry-induced flows on endothelial cell behavior in 3D printed small-diameter blood vessels

Sung Yun Hann ^a, Haitao Cui ^a, Nora Caroline Zalud ^a, Timothy Esworthy ^a, Kartik Bulusu ^a, Yin-Lin Shen ^a, Michael W. Plesniak ^{a,c}, Lijie Grace Zhang ^{a,b,c,d,*}

- ^a Department of Mechanical and Aerospace Engineering, The George Washington University, Washington, DC 20052, USA
- b Department of Electrical and Computer Engineering, The George Washington University, Washington, DC 20052, USA
- Department of Biomedical Engineering, The George Washington University, Washington, DC 20052, USA
- ^d Department of Medicine, The George Washington University Medical Center, Washington, DC 20052, USA

ARTICLE INFO

Keywords: 3D printing Blood vessel Geometry Endothelial cells Dynamic flows

ABSTRACT

Clinical recovery from vascular diseases has increasingly become reliant upon the successful fabrication of artificial blood vessels (BVs) or vascular prostheses due to the shortage of autologous vessels and the high incidence of vessel graft diseases. Even though many attempts at the clinical implementation of large artificial BVs have been reported to be successful, the development of small-diameter BVs remains one of the significant challenges due to the limitation of micro-manufacturing capacity in complexity and reproducibility, as well as the development of thrombosis. The present study aims to develop 3D printed small-diameter artificial BVs that recapitulate the longitudinal geometric elements in the native BVs using biocompatible polylactic acid (PLA). As their intrinsic physical properties are crystallinity dependent, we used two PLA filaments with different crystallinity to investigate the suitability of their physical properties in the micro-manufacturing of BVs. To explore the mechanism of venous thrombosis, our study provided a preliminarily comparative analysis of the effect of geometry-induced flows on the behavior of human endothelial cells (ECs). Our results showed that the adhered healthy ECs in the 3D printed BV exhibited regulated patterns, such as elongated and aligned parallel to the flow direction, as well as geometry-induced EC response mechanisms that are associated with hemodynamic shear stresses. Furthermore, the computational fluid dynamics simulation results provided insightful information to predict velocity profile and wall shear stress distribution in the geometries of BVs in accordance with their spatiotemporally-dependent cell behaviors. Our study demonstrated that 3D printed small-diameter BVs could serve as suitable candidates for fundamental BV studies and hold great potential for clinical applications.

1. Introduction

The main scope of tissue engineering includes the successful generation of artificial tissues and organs to fully restore their original functions [1]. According to the recent statistics of the American Heart Association in 2021, the leading causes of death in the US are heart and vascular diseases, such as cardiovascular, venous, and artery diseases [2]. In other words, hundreds of thousands of annual deaths in the US are related to vascular diseases. Hence, blood vessel (BV) diseases including atherosclerosis (plaque localization), and thrombosis remain as unsolved major vascular diseases [3–6]. In the human body, BVs are

responsible for nutrition and oxygen transport as well as waste removal to maintain metabolism [7,8]. Although different types of cells possess different sensitiveness to oxygen, in extreme cases, most cells can survive only within a range of 200 μ m from their closest BV [9,10]. Moreover, sufficient vascularization is the key to successfully fabricating artificial tissues and organs for clinical application. To remedy BV diseases, autologous vessels have been considered the standard treatment [6,11]. However, the limited number of autografts is a great obstacle for patients to overcome [11]. Consequently, artificial vessels with large-diameter (>8 mm) and medium-diameter (6–8 mm) to replace general arteries or veins were developed along with the studies associated with

^{*} Corresponding author at: Department of Mechanical and Aerospace Engineering, The George Washington University, Science and Engineering Hall 3590, 800 22nd Street NW, Washington, DC 20052, USA.

E-mail addresses: shann008@gwmail.gwu.edu (S.Y. Hann), htcui@email.gwu.edu (H. Cui), caroline_zalud@gwmail.gwu.edu (N.C. Zalud), tesworthy@email.gwu.edu (T. Esworthy), bulusu@gwu.edu (K. Bulusu), yshen@gwu.edu (Y.-L. Shen), plesniak@gwu.edu (M.W. Plesniak), lgzhang@email.gwu.edu (L.G. Zhang).

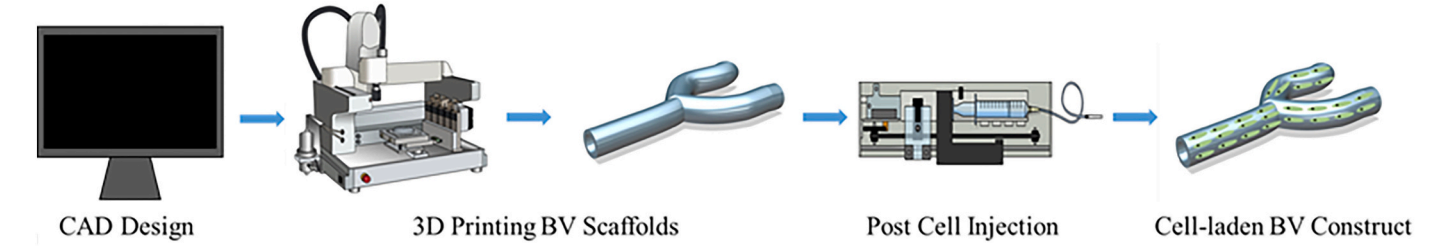


Fig. 1. A schematic illustration of the overall BV fabrication process.

artificial tissues [12-14]. However, the fabrication of small-diameter (<6 mm) artificial vessel implants remains as a significant challenge due to the difficulty of precise microfabrication and integration with their surrounding tissues. In addition, the failures of small-diameter vessel implants are generally related to poor patency, caused by the development of thrombosis as a result of the inadequate reendothelialization in the artificial vessel lumen [3,12,15-17]. Also, researchers have mostly focused their efforts on studies associated with arteries, as the development of atherosclerosis (plaque localization) is most common in the arterial system and has been widely studied [3-5]. However, the relevant fundamental studies of veins are not as abundant as arteries, although thrombosis appears in both arteries and veins [17]. Venous diseases consist of two major classifications, which are blockage (thrombosis) and deficient drainage [17]. As an essential component of BV, the endothelium plays a significant role in the regulation of vascular integrity and progression of thrombosis (blood clots) as it is primarily exposed to blood flow [18-20]. Also, most BV-related diseases occur on the endothelium by local plaque (e.g., cholesterol and fat) deposition, especially at the bifurcation regions [21]. It is known that endothelial cells (ECs) are the fundamental components of the endothelium in the innermost layer of the human BVs from capillaries to arteries and veins. Their pathophysiological behaviors such as adhesion, morphology, cytoskeletal organization, migration, and functions are significantly affected by geometry-induced complex hemodynamic flows [7,8,22]. Thus, it is necessary to perform a feasibility study of geometric effects on the endothelialization to understand the fundamental mechanism of thrombosis, which is a primary step toward the successful fabrication of artificial BVs.

Among the various efforts to create biomimetic artificial tissues, 3D printing has been considered one of the most promising fabrication technologies due to its advantages in controllability, repeatability, and reproducibility [23,24]. There have been many studies related to the design and the fabrication of specific artificial tissues reported, including artificial bone [23,25], skin [26,27], cartilage [28,29], and cardiac tissues [30,31]. Among different printing technologies, fused deposition modeling (FDM) is advantageous for manufacturing artificial vessel implants or replacements as it offers: 1) a broad selection for biocompatible printing materials approved by the FDA for other biomedical applications, 2) a cost-effective fabrication process with high-quality control, 3) a relatively rapid and reliable printing process, 4) an easy-to-clinical translation solution, and 5) the essential characteristics to match the basic requirements for artificial vessels [24,32,33]. As a widely accepted material of artificial BVs, polylactic acid (PLA) is a biocompatible synthetic biopolymer, a prevalent 3D printing filament used for various biomedical applications due to its outstanding biodegradability, biocompatibility, and processability [7,32,34–36]. With the rising demand for FDM 3D printing, selections of commercially available PLA filaments have also been diversified, especially with respect to their intrinsic physical properties. Through annealing, adjusting the stereoisomerism, or adding the nucleating agents, PLA filaments with different crystallinity ranging from an amorphous glassy state to a semicrystalline state and highly crystalline state are obtained. The crystallinity of PLA also significantly affects its material properties, such as optical properties (transmittance or visibility), thermal properties (glass

transition and melting temperature), degradability, and mechanical properties (Young's modulus and yield strength) [37,38]. Hence, it is also worth investigating and optimizing crystallinity-dependent properties of PLA filaments to provide insightful information for 3D printing of artificial vessel implants.

In this study, we specifically focused on the effect of material crystallinity in the 3D printed small-diameter artificial BV implants, in which the effect of geometry-induced flows on the cellular behavior of ECs was further explored. Specifically, biomimetic 3D printed BV models including disturbed and unidirectional laminar flow regions with a monolayer vascular bed were created. In order to select an ideal 3D printing PLA filament for the vessel fabrication, low crystalline (LC) and high crystalline (HC) PLA filaments, which possess the lowest and highest material crystallinities (0.93 \pm 0.06% and 5.05 \pm 0.18%, respectively), were chosen for physical characterization [37]. Then, 3D printed small-diameter BV implants with three different geometrical characteristics that recapitulate the longitudinal geometric elements in the native BVs were fabricated to visually characterize and quantify EC activities in a physiologically dynamic flow environment. Also, the spatial wall shear stress (WSS) distributions of different BV geometries were calculated using computational fluid dynamics (CFD) for potentially predicting their behavior in vivo.

2. Materials and methods

All solvents and reagents were purchased from Sigma-Aldrich (St. Louis, MO), unless otherwise specified.

2.1. Optimization of 3D printable filament materials

2.1.1. 3D printing of samples

All 3D models were created with the Autodesk 123D (Autodesk, Inc., San Rafael, CA) computer-aided design (CAD) software and exported to an FDM 3D printer (MakerBot, Brooklyn, NY) in the form of an STL file to extrude LC and HC PLA filaments (FilamentDirect, Nashville, TN) at 215 °C (Fig. 1). The PLA filaments used in this study possessed the average molecular weights (M $_{\rm w}$) and dispersity (Đ) around 70 kDa and 1.38 for LC and around 85 kDa and 1.5 for HC. Discs (8 mm \times 1 mm) (D \times H) or straight (ST) BV implants with a dimension of 2 mm in inner diameter and 10 mm in length were first evaluated to investigate the physical properties and cytocompatibility of the materials.

2.1.2. In vitro enzymatic (EZ) and non-enzymatic (NE) biodegradation quantification

To test the biodegradability of both LC and HC PLA filaments, 3D printed PLA discs were prepared. For an EZ biodegradation test, a lipase (isolated from porcine pancreas, EC 3.1.1.3) phosphate buffer saline (PBS) solution at a concentration of 75 mg/mL was used, while NE biodegradation was performed in pure PBS, as lipase is known to be the most compatible degrading enzyme for PLA [39–41]. The completely sealed solutions with the samples were left in a water bath at 37 °C for up to 20 days. The buffer solutions were changed every other day to maintain freshness. The samples of the four groups were dried in an oven at 80 °C for 90 min and cooled at room temperature for 60 min prior to

the measurement. Weight loss of each group was evaluated on days 1, 5, 10, and 20 and calculated using the following equation [39,41].

Weight loss (%) =
$$\frac{w_i - w_f}{w_i} \times 100$$
 (%)

2.1.3. Mechanical property quantification and surface characterization

To compare the mechanical properties of samples before and after degradation, four major experimental groups of 3D printed PLA BV samples, including LC-EZ, LC-NE, HC-EZ, and HC-NE, were prepared. In each group, compression and tension tests were conducted for all the samples that were biodegraded in the same setup described above for 0, 10, and 20 days using an MTS Criterion universal testing system with a 100 N load cell equipped (MTS Systems Corp, Eden Prairie, MN). For the tension test, the BV samples were mounted on the clamps and pulled at a rate of 2 mm/min until failure. Young's modulus was calculated from the linear portion of the tensile stress-strain curve. For the compression test, the BV samples were compressed at a strain rate of 10 mm/min with a preload of 0.01 N to provide initial contact between the loading plate and the scaffolds. The compressive modulus of each sample was obtained from the slope of the linear elastic region between 0 and 10% of the stress-strain curve.

The surface topography comparisons of the samples before and after degradation were evaluated by an FEI Teneo LV Scanning electron microscope (SEM) (Thermo Fisher Scientific, Waltham, MA). Prior to the exposure to a 5 kV potential difference with a 0.2 nA–13 pA electron beam for imaging, each sample was coated with a 3 nm thick layer of argon [23].

2.1.4. Cell culture

Human umbilical vein endothelial cells (ECs) obtained from Thermo Fisher Scientific (Waltham, MA) were used in this study. ECs were cultured in endothelial growth media (EGM) (Cell Applications, Inc., San Diego, CA). All experiments were performed with ECs of a single-digit passage number, and EGM was changed every day.

2.1.5. In vitro cytocompatibility quantification

To quantify the cell proliferation on both LC and HC PLA, the ECs were seeded at a density of 1000 cells/mm^2 on LC and HC PLA discs and cultured in 48-well plates (VWR International, Randor, PA) in a cell culture incubator at 37 °C with 5% CO₂ concentration. Blank polystyrene 48-well plates without a PLA disc served as a control, and EGM was replaced every day. The cell proliferation was quantified after 1, 4, and 7 days of culture using a cell counting kit (CCK-8, Dojindo Molecular Technologies, Japan). The cell counting solution consisted of 10% (v/v) CCK-8 reagent and 90% (v/v) EGM. $400 \, \mu\text{L}$ of the cell counting solution was added to each well, and then incubated at 37 °C with 5% CO₂ concentration for 3 h prior to the quantification. $200 \, \mu\text{L}$ of supernatants from each well were transferred into a 96-well plate, and the absorbance of the solution was assessed at 450 nm using a Multiskan GO Spectrophotometer (Thermo Fisher Scientific, Waltham, MA) [23].

2.2. Evaluation of cellular behavior in 3D printed BV implants

2.2.1. Designing and printing of 3D small diameter BV implants

To recapitulate the longitudinal geometric elements in the native BVs, an intact small-diameter artificial BV implant (2 mm inner diameter with 0.5 mm wall thickness) with three different geometrical characteristics, including straight (ST), 45-degree curved arc (CV), and Y-shape (YS), was designed, and then FDM 3D printed with LC PLA filament. To investigate the effects of geometry-induced flows on EC behavior, the same three different types (ST, CV, and YS) of BV implants were also designed and printed.

2.2.2. In vitro hemodynamic flow system

Similar to our previously performed study [23], a customized

bioreactor system was developed to establish a dynamic cell culture environment, which resembles an *in vivo* microcirculation. EGM was supplied by a fluid reservoir and perfused by a digital peristaltic pump (Cole-Parmer, Vernon Hills, IL) to continuously pass through the 3D BV channels at a flow rate of 2 mL/min. The entire setup was then transferred in a cell culture incubator at 37 $^{\circ}\text{C}$ and 5% CO $_2$ concentration. Also, 300 mL of the EGM was completely changed to a fresh one every 3 days.

2.2.3. F-actin and immunofluorescence staining

The morphology and alignment of ECs were visually evaluated after 1, 4, and 7 days of dynamic culture using F-actin staining, and images were obtained with a Zeiss LSM 710 confocal microscope (Carl Zeiss AG, Oberkochen, Germany). Also, the ImageJ software was used to analyze and to calculate cell alignment angles with respect to the flow direction. ECs at a density of 1000 ECs / mm2 were seeded on LC PLA discs. Each BV implant was rinsed three times with PBS, and the adhered ECs were fixed and permeabilized for 15 min using 10% formalin and 0.1% Triton X-100 solutions, respectively. After the samples were washed three times once again, the cytoskeleton of the ECs was stained with Texas red $^{\text{TM}}$ -X phalloidin fluorescent dye (Invitrogen, Carlsbad, CA) in red for 1 h, and the nuclei of the ECs were stained with 4',6-diamidino-2-phenylindole dihydrochloride (DAPI) (Invitrogen, Carlsbad, CA) in blue for 15 min.

Furthermore, immunostaining was performed after 1 and 2 weeks of dynamic cell culture to investigate the expression of specific proteins of ECs in the 3D printed BV implants. The same protocol for our previous vascularization study was used to fix and to permeabilize the adhered cells and to block non-specific antibody binding [23]. Upon the removal of the blocking solution and PBS washing, the scaffolds were incubated overnight at 4 °C with the primary antibody, including anti- a cluster of differentiation 31 (CD31) (Abcam, Cambridge, UK) and anti-VE cadherin (CD 144) (Thermo Fisher Scientific, Waltham, MA). Following that, the thoroughly rinsed scaffolds were incubated for 1 h at room temperature in goat anti-rabbit IgG H&L (Alexa Fluor® 488) (Abcam, Cambridge, UK). Then, the immunofluorescence-stained samples were imaged using the confocal microscope.

2.2.4. Computational simulation to determine BV lumen WSS

The BVs with three geometries were designed using ANSYS® Design Modeler (ANSYS, Inc., Canonsburg, PA). According to the physical properties of PLA, they were assumed to have rigid walls with no-slip boundary conditions, and the same dimensions and flow rate were applied as in the experimental study described above. The inlet condition was modeled by a fully developed parabolic velocity profile, whereas the outlet was prescribed as a zero-pressure outlet. ANSYS® FLUENT Academic Research Mechanical Release 2021 R1 was used to solve the Navier-Strokes equations employing a finite volume method. To model the flow through the different vessel geometries, a pressurebased solver under steady laminar flow conditions was utilized. ANSYS® meshing tool and ANSYS® FLUENT were used to discretize the domain and post result processing, respectively. The rheological properties of the model fluid (EGM) were approximated by those of water at 37 °C having Newtonian fluid behavior, where density and dynamic viscosity were prescribed accordingly [42-44]. The accuracy of wall shear stress (WSS) calculations, as well as the discretization independence of the results were validated for the ST BV implants using the theoretical Hagen-Poiseuille law:

$$WSS_{theory} = \frac{4\mu Q}{\pi R^3}$$

where Q, μ , and R are the volumetric flow rate, the dynamic viscosity, and the BV radius, respectively. Computational results show a very high accuracy as they are within 0.1% of the analytical ones. For the CV and YS BVs, the results were validated via a mesh independence study. The

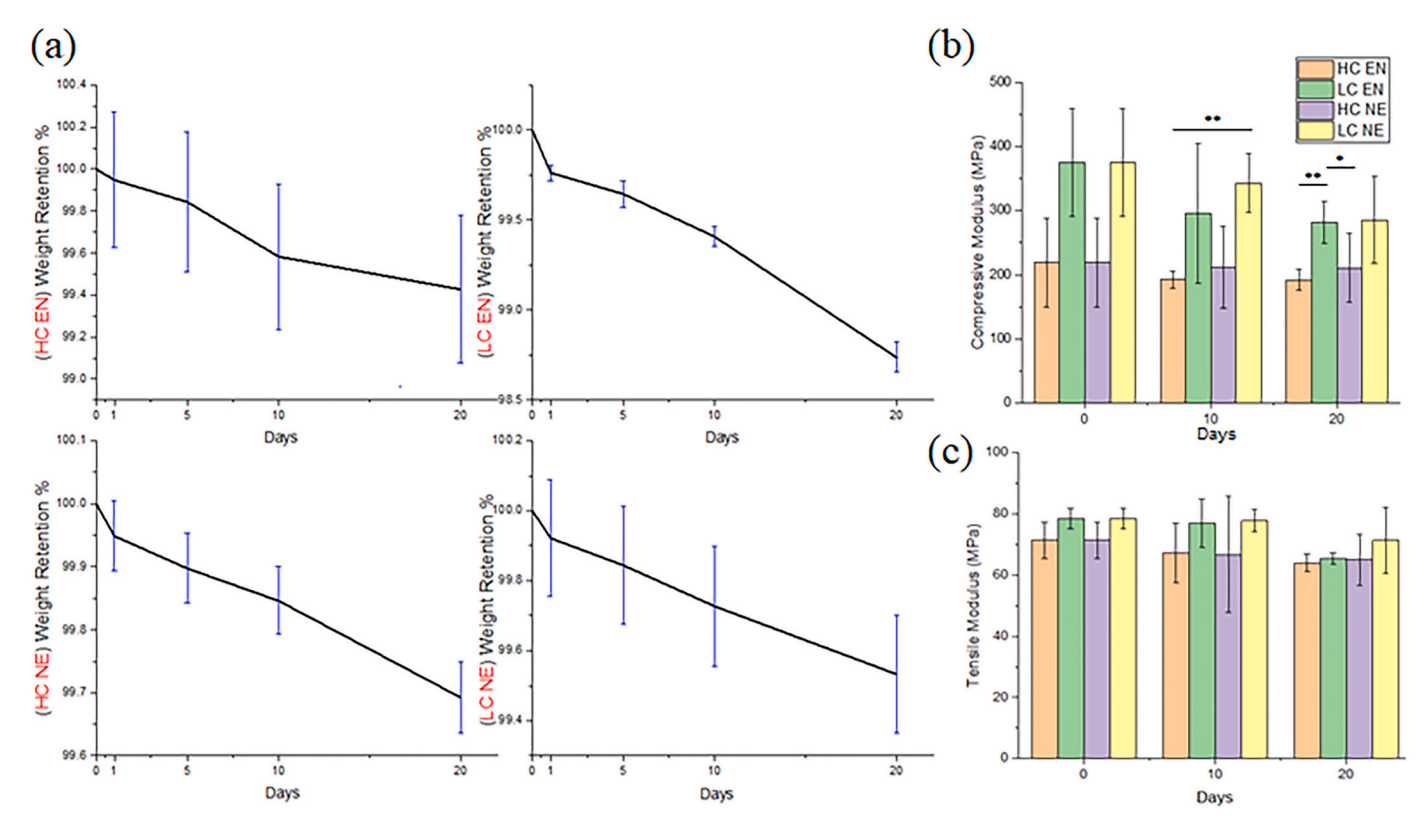


Fig. 2. (a) Quantification results of biodegradability for LC and HC PLA discs in lipase-enzymatic (EZ) and non-enzymatic (NE) solutions up to 20 days. HC-EN, LC-EN, HC-NE, and LC-NE PLA samples in a clockwise rotation. (b) Compressive and (c) tensile modulus of HC-EN, LC-EN, HC-NE, and LC-NE PLA samples on initial, 10, and 20 days. *p < 0.05 and *p < 0.01.

CFD investigation was used to analyze and quantify the effect of BV geometries on the spatial distribution and average WSS. Flow characteristics were prescribed by the Reynolds number:

$$Re = \frac{uD\rho}{\eta}$$

where u, D, ρ , and η indicate the flow velocity, vessel diameter, fluid density, and dynamic viscosity, respectively. Based on our model, a fixed Reynolds number of 30.6 was used for both experimental and numerical setups.

2.3. Statistical analysis

All quantitative data are presented as the mean \pm standard deviation (n = 9). Data were analyzed by one-way analysis of variance (ANOVA) method to verify statistically significant differences among experimental groups. A *p*-value < 0.05 was taken to be statistically significant.

3. Results and discussion

3.1. Biodegradability and mechanical properties

To select an optimal PLA filament for the artificial vessel printing, the excellent mechanical tolerance and proper biodegradation rate of materials were primarily considered. The biodegradability of LC and HC PLA discs was evaluated in EZ and NE solutions for up to 20 days. Among various degradation mechanisms, the biodegradation of PLA is associated with the reorganization of polymers into water and carbon dioxide, triggered by enzymes or microorganisms in the body [41,45]. Additionally, there are several physical properties significantly affecting the biodegradability of polymers, including crystallinity, molecular conformation, and molecular weight [46]. It was found that LC PLA

filament presented a higher degree of weight loss compared to the HC PLA group in both EN and NE conditions (Fig. 2a). The weight loss became more pronounced as time passed in four different groups. Specifically, the LC group exhibited 1.26% and 0.46% weight loss over 20 days. Considering the polar opposite crystallinities of the LC and HC PLA filaments, the experimental results demonstrated that both the presence of enzyme and crystallinity were apparently responsible for PLA biodegradation in our study. Considering EN environment in the human body, use of LC PLA for artificial BV is advantageous, as it appeared to possess relatively rapid degradation rate, then it can be promptly replaced with regenerated vessels.

The mechanical tolerance of systemic arterial pressures is crucial for the clinical application of artificial vessels in a long-term dynamic flow environment. To further compare the mechanical properties of LC and HC PLAs during the biodegradation process, compressive and tensile moduli of the samples were evaluated. For the modulus tests, BV implants (2 mm \times 1 mm \times 10 mm) (Diameter \times Wall thickness \times Length) were 3D printed and immersed in the EN and NE solutions for the same period. It was found that both (EN and NE) groups of the LC PLA BV implants possessed higher compressive moduli than the HC PLA samples at every time point (Fig. 2b). Specifically, the difference in compressive modulus between LC and HC PLAs in the EN condition was around 156 MPa (initial), 103 MPa (10 days), and 90 MPa (20 days). The tensile moduli of the BV implants exhibited a similar but slightly different pattern (Fig. 2c). The general tendency was consistent with the results of compressive modulus testing, where LC PLA BV implants maintained a higher mechanical durability over time. However, the discrepancy in values of tensile modulus between LC and HC samples became much smaller, approximately 7.2 MPa (initial), 9.7 MPa (10 days), and 1.4 MPa (20 days) for the EN condition. The explanation is that the existence of enzymes affects the duration of biodegradation for PLA and is more significant to the PLA samples with higher crystallinity [41]. Prior to the

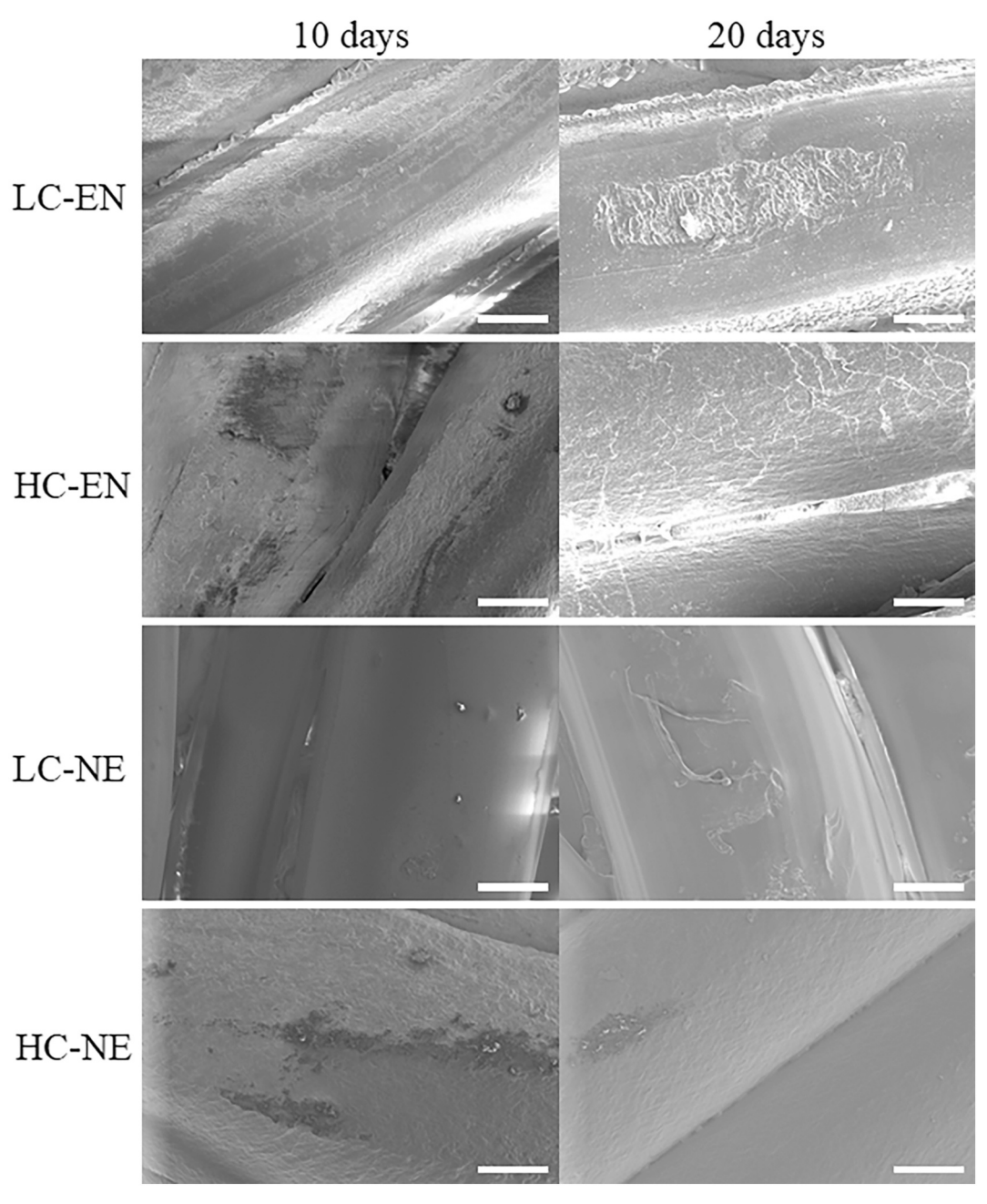


Fig. 3. SEM images of LC and HC PLA BV samples after 10 (left column) and 20 days (right column) of the EN and NE biodegradation. Due to the presence of lipase, hydrolysis appeared to be accelerated in the EN group. Scale bars, 100 μm.

biodegradation process, PLA with higher crystallinity (HC samples in our study) first experiences a bio-deterioration step, which is the consequence of the microorganism spearing throughout the samples [41,47,48], leading to slower biodegradation than the LC samples. This experimental result shows that the innate durability of the LC PLA samples was greater than that of the HC PLA samples, which is similar to the previously reported study [37]. However, the discrepancy between LC and HC PLA groups tended to gradually decline with the progression of the biodegradation, as expected. The results indicate that there is a clear advantage to using LC PLA filament rather than HC PLA to ensure mechanical tolerance of artificial vessels, especially in complex *in vivo* environments.

3.2. Surface morphology and cell proliferation

The surface morphology of 3D printed LC and HC PLA samples after

10 and 20 days of biodegradation was characterized (Fig. 3). It was observed that the natural surface of the HC PLA samples was rougher than that of the LC PLA samples. Also, the visual difference between 10 and 20 days within the same group was more evident in the EN environment due to the presence of lipase, which accelerates enzymatic hydrolysis of PLA [41]. In addition, cell proliferation of ECs on the 3D printed LC and HC PLA scaffolds were quantified on 1, 4, and 7 days (Fig. 4a), where a polystyrene 48-well plate served as a control. The results showed that LC PLA implants have higher cell proliferation than the HC PLA samples, although the well plate exhibited the highest cell proliferation. However, the cells seeded on the LC PLA samples possessed the most accelerated proliferation rate across all the experimental and control groups. This is because the surfaces of 3D printed scaffolds yield a larger surface area due to the presence of microgrooves, whereas the well-plate has a perfect 2D surface. Generally, our results suggested that the physical and biological properties of 3D printing PLA

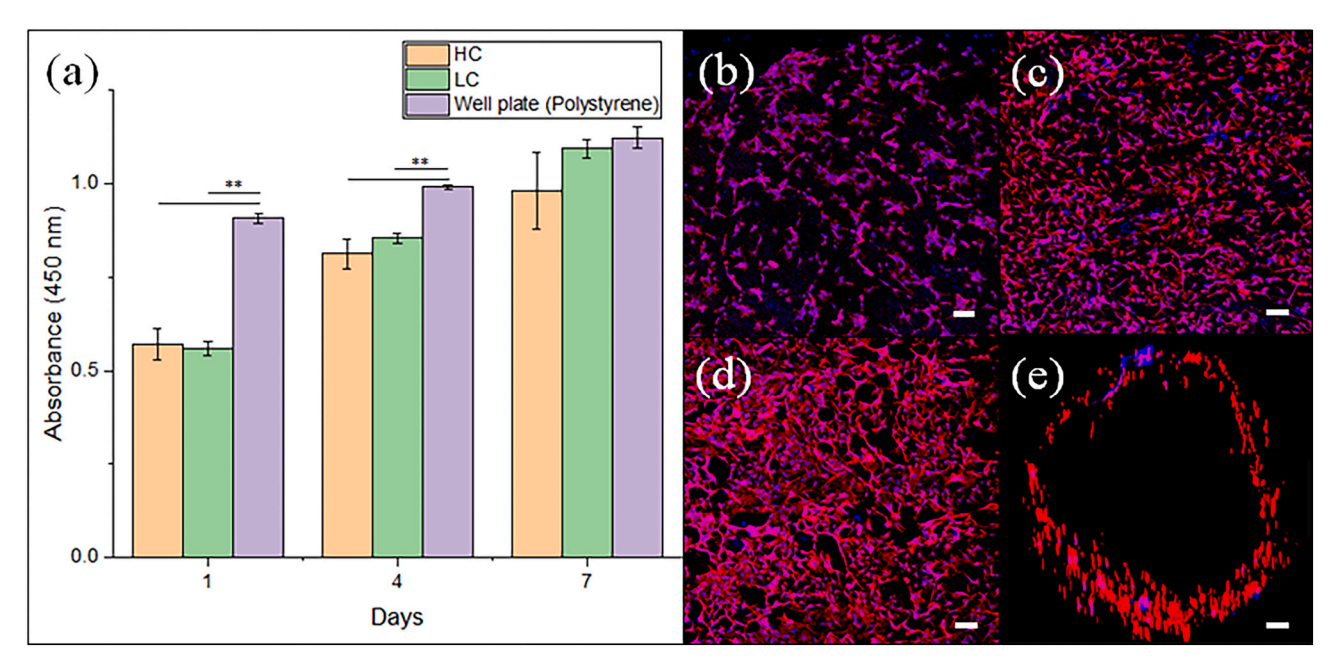


Fig. 4. (a) Quantification of cell proliferation of ECs on the fabricated HC and LC PLA BV implants with a well plate as control after 1, 4, and 7 days. **p < 0.01. (b–d) Confocal microscopic images of ECs seeded on the printed LC PLA BV implants after 1, 4, and 7 days, respectively. Scale bars, 200 μ m. (e) A confocal cross-sectional microscopic image of EC distribution in the printed BV implants after 4 days of cell culture. Scale bar, 100 μ m.

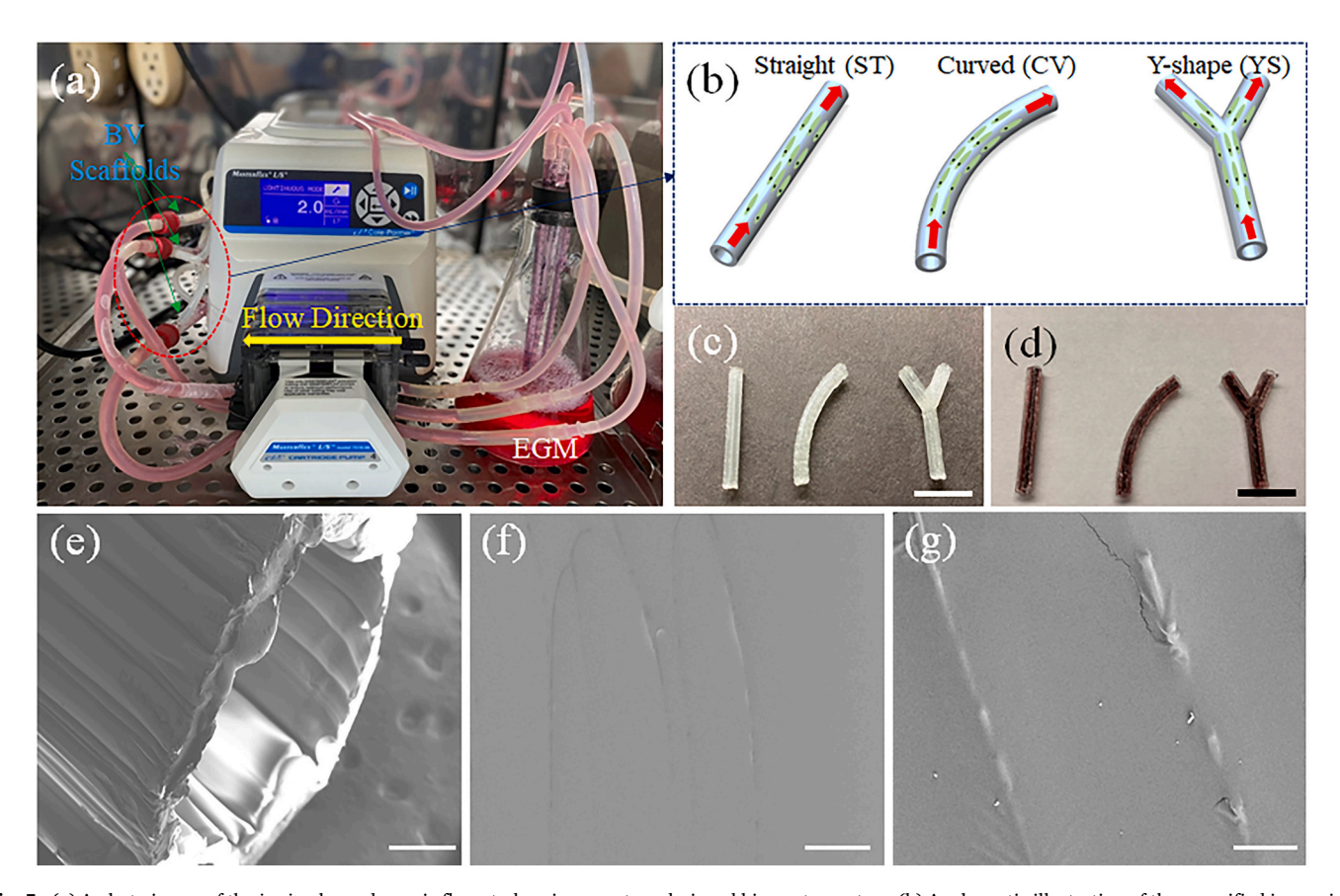


Fig. 5. (a) A photo image of the *in vitro* hemodynamic flow study using a custom-designed bioreactor system. (b) A schematic illustration of the magnified inner view of BV implants with different geometries (ST, CV, and YS) for the dynamic cell culture. The 3D printed LC PLA BV implants (c) before and (d) after red dye injection to mimic the blood perfusion *in vivo*. Scale bars, 1 cm. (e) An SEM cross-sectional image of the 3D printed BV implant. Scale bar, 500 μ m. SEM images of the lumen of the 3D printed BV implant at high magnifications, such as (f) \times 2000 (scale bar, 50 μ m) and (g) \times 10,000 (scale bar, 10 μ m). (For interpretation of the references to color in this figure legend, the reader is referred to the web version of this article.)

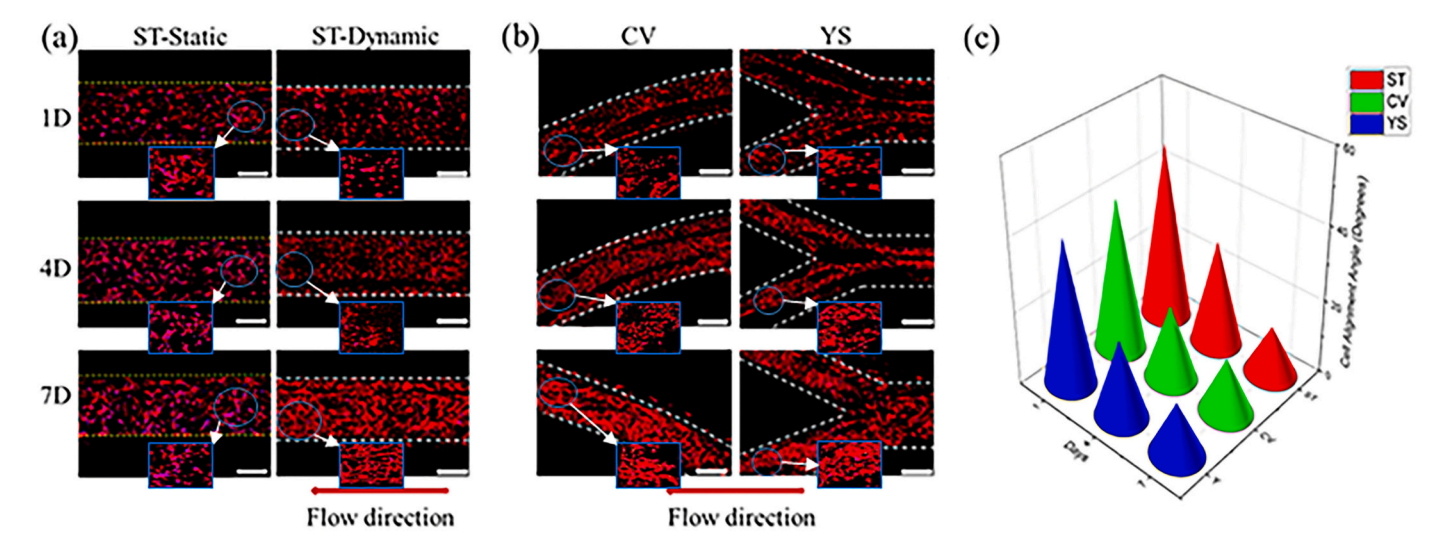


Fig. 6. (a) Confocal microscopic images of F-actin staining of ECs cultured in printed ST vessels in the static and dynamic culture conditions after 1, 4, and 7 days. Scale bars, 1 mm. (b) Confocal microscopic images of F-actin staining of ECs cultured in CV and YS vessels in the dynamic culture condition after 1, 4, and 7 days. Scale bars, 1 mm. (c) An analysis of cell alignment angles in each group after 1, 4, and 7 days.

filaments are crystallinity-dependent, and LC PLA filament is an optimal selection to fabricate the artificial BV implants. Therefore, the cell morphology was also visually evaluated to observe the EC adhesion and growth on the LC PLA for 7 days. As shown in Fig. 4b–d, the separated ECs proliferated to reach an optimal confluence and gradually assembled into a monolayered endothelium, which also demonstrated the cytocompatibility of the LC PLA scaffolds. In addition, successful lumen formation, which is an essential process to create a functional BV was observed after 4 days (Fig. 4e).

3.3. Geometry-induced flow effects on cell alignment and morphology

It is known that significant changes in phenotype and function of native endothelium are caused by the mechanical forces of blood flow [49,50], particularly by the WSS; therefore, it is crucial to systematically explore the role of geometry-induced flows on endothelial cell responses in the 3D artificial vessel models. After the selection of optimal PLA filaments, LC BV implants with different geometries (including ST, CV, and YS, which are representative of universal BV shapes in the human body) were 3D printed to further investigate cell behavior in a dynamic flow condition using a custom-designed bioreactor system (Fig. 5a-d). The continuous flow rate was set at 2 mL/min throughout the entire culturing period to mimic the native condition in the human body, and SEM images showed the cross-sectional architecture of the vessel and the micro-structure of the lumen (Fig. 5e-g). According to a previously reported study, the blood flow rate with a BV channel diameter of around 2 mm is within the range of 1.2-4.8 mL/min in BVs of the human body [51]. Meanwhile, ECs seeded in a set of ST-LC BV implants in a static culture condition served as a control. As shown in Fig. 6a, F-actin cell staining images monitored for 1, 4, and 7 days indicated that the cell culture environment, i.e., shear stress, significantly affected cytoskeleton characteristics of the ECs, including structure and organization. The cell alignment and orientation of the characteristic region in each cell staining image were analyzed using the ImageJ software. Interestingly, there were slight changes in cell alignment angles and morphologies for the three different dynamic groups (ST, CV, and YS) until day 4. The distinctive alignment changes became apparent on day 7, on which the adhered ECs appeared to be elongated and aligned parallel to the flow direction (Fig. 6b), whereas the cells cultured in the static condition did not exhibit regularly aligned morphologies over the same time intervals. Based on the analysis of 10 randomly selected regions in each group, it was noticed that the angles between the cells and the flow

direction decreased from around 45° (1 day) to 15° (7 days) after the exposure to the EGM perfusion (Fig. 6c). This result demonstrated that the adhered healthy cells were elongated along the flow direction, suggesting that the development of a mature endothelium would be enhanced in the in vivo resembling environment. Moreover, it was established that micropatterning of the cytoskeletal axis of ECs in a laminar flow was also dependent on the BV implant's geometry and flow direction. The results demonstrated that the existence of the bifurcation region causing a disturbed flow could be thrombogenic. It is reported that the ECs were considerably more sensitive to relatively low shear stresses in disturbed flow [52], which was induced by geometry (bifurcation) in our study. Therefore, we observed that ECs were unable to be well attached or aligned at high angles to the flow direction at the bifurcated region, leading to the low multi-directional shear stressinduced cell retraction (morphology change, loss of contact inhibition of growth, and even detachment of cells) compared to the BV implants with a unidirectional laminar flow [52,53]. The resultant endothelial dysfunction could result in various non-adaptive alterations in functional phenotype, which plays an important role in the regulation of hemostasis and thrombosis, local vascular tone and redox balance, and the orchestration of acute and chronic inflammatory reactions [54].

3.4. Computational investigation of BV geometry-dependent flow field and WSS

As the flow field within the vessel is fundamentally determined by its geometry, a velocity magnitude contour plot along the BV diameter center plane was created (Fig. 7a-c). In all three geometries (ST, CV, and YS), the flows at the inlets were equal with the highest velocity magnitudes at the BV centerline and zero velocity at the vessel wall. WSS spatial distributions for the same geometries were also analyzed (Fig. 7d-f). In agreement with the analytical value for this canonical case, the ST BVs exhibited a constant WSS value of 0.29 dyn/cm² (Table 1). In the CV BVs, the velocity profile deformed due to the vessel curvature and the corresponding radial pressure gradients, which resulted in higher (and lower WSSs) in the inner (and outer) walls, as expected (Fig. 7g) [55,56]. The low Reynolds number and the large BV curvature radius explained the very narrow range of WSS values present in the CV BVs. This phenomenon was further supported by a very similar velocity vector field and magnitudes for both ST and CV BVs. Likewise, computed average WSSs for the ST and CV BVs were found to be approximately equal, only varying by a relative difference of 0.1%. The

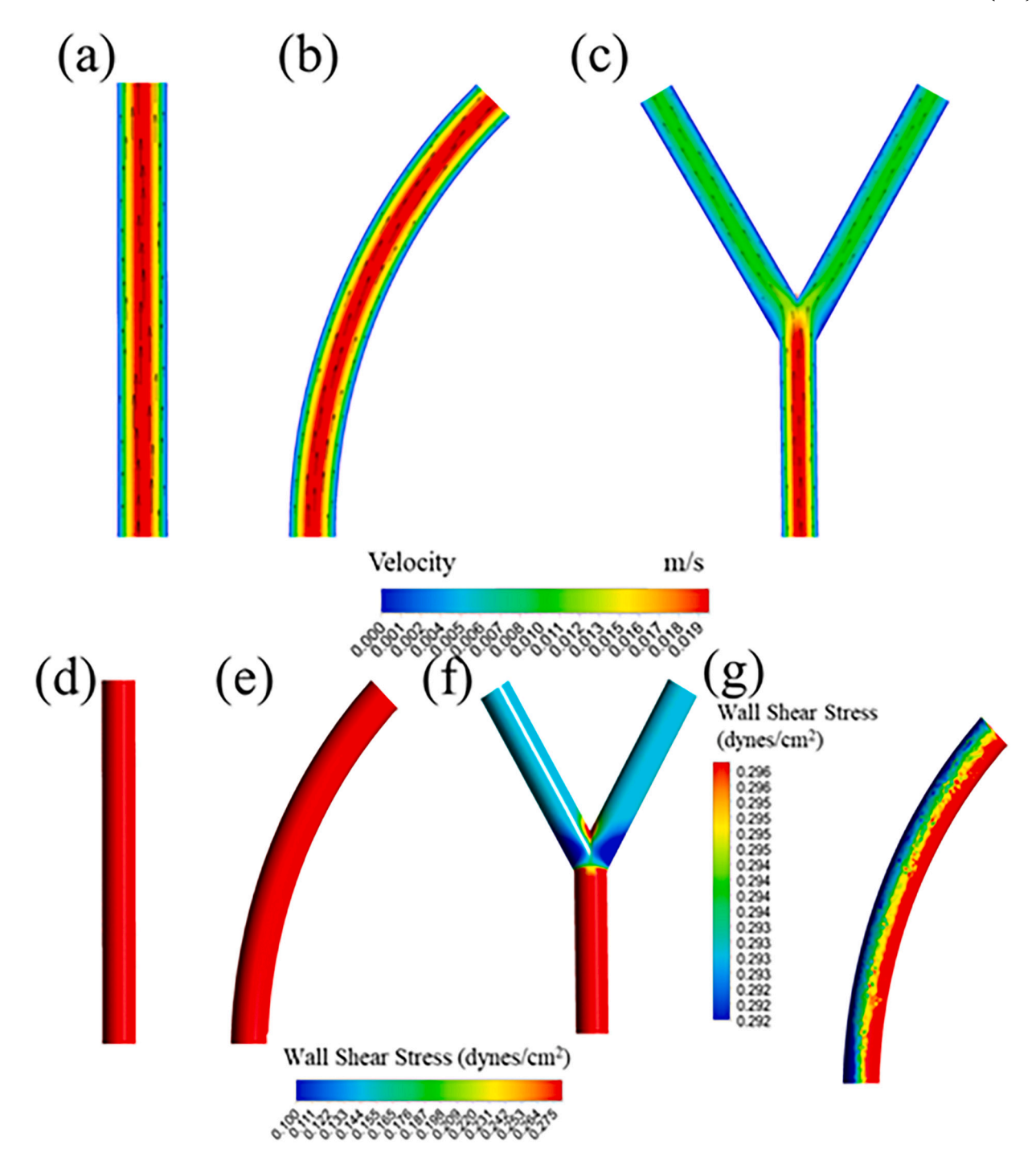


Fig. 7. A velocity magnitude contour plot for the BVs with three different geometries, including (a) ST, (b) CV, and (c) YS. All the groups exhibited zero and max velocities at the wall and the center, respectively. The black arrows indicate velocity direction, and their lengths are scaled to magnitude. The wall shear stress (WSS) distribution for (d) ST, (e) CV, and (f) YS BVs. (g) The WSS distribution along the lumens in the CV BVs. The bifurcation in the YS BVs exhibited a halved volume flow through each branch and lower velocity flow separation zones at the outer walls.

 $\begin{tabular}{ll} \textbf{Table 1} \\ \textbf{Area-averaged WSSs along the BV lumen and the relative difference among the three geometries.} \\ \end{tabular}$

Geometry	Area-weighted average WSS (dyn/ cm ²)	Comparison between BVs	Relative difference of weighted average WSS (%)
ST	0.294	ST vs. CV	0.11
CV	0.295	CV vs. YS	34.6
YS	0.193	ST vs. YS	34.5

computed flow in the YS BVs exhibited higher local deviations in WSS than the CV BVs, caused by the low velocity of flow separation zones at the bifurcation onset. The volumetric flow rate was halved in each of the YS BVs branches so that the inlet and the bifurcated vessel branches experienced a higher and a lower WSS respectively, leading to a 35% difference in average WSS between the YS BV and the ST and CV BVs. These results demonstrated that vessel bending and curvature, or an abrupt shape modification induced substantial changes in WSS in the BVs. Furthermore, this computational simulation helps to explain the cell experiment results that exhibited the lack of adhesion and

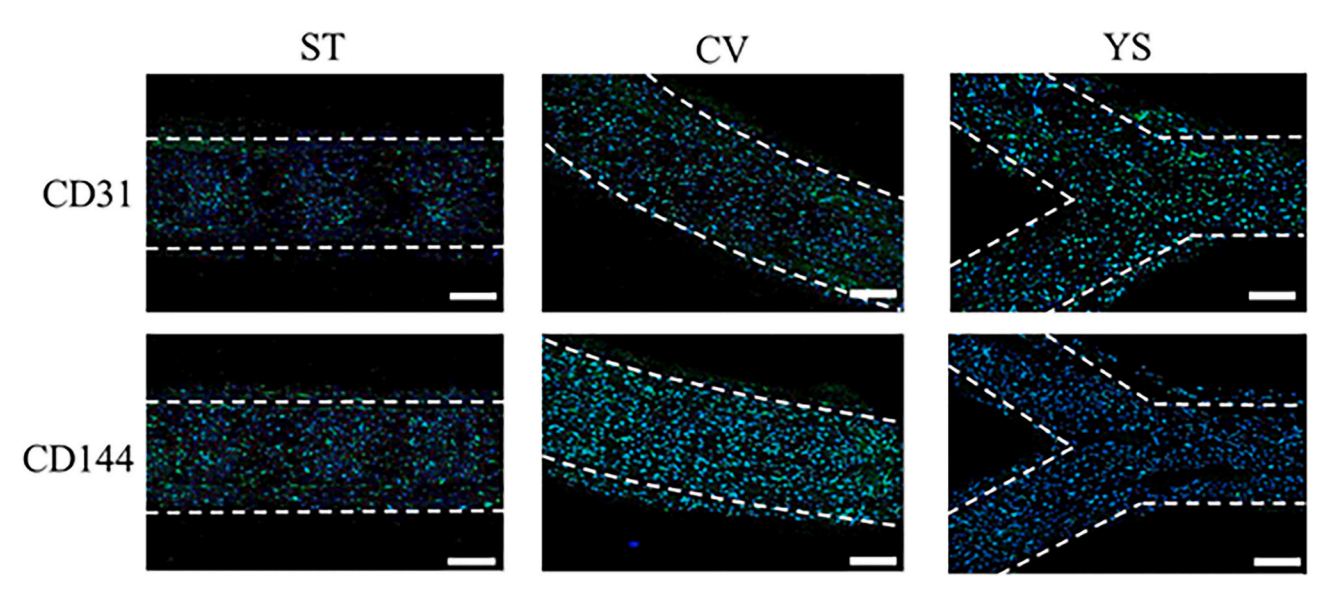


Fig. 8. Confocal immunofluorescence images of 3D printed BV implants with ECs in the dynamic culture conditions after 2 weeks. CD31 (green) and CD144 (VE-cadherin, green) with DAPI (blue) were used to engage the vascular-specific expression of ECs. Scale bars, 1 mm. (For interpretation of the references to color in this figure legend, the reader is referred to the web version of this article.)

cytoskeleton microfilament arrangement, especially in the bifurcated region caused by disturbed flow.

3.5. Effect of geometry-induced flows on vasculogenesis in the 3D printed BV implants

To further evaluate the maturation of endothelial function, the immunocytochemistry of the formed endothelium in the 3D printed BV implants was visually evaluated with the staining of EC-specific biomarkers, including CD31 and CD144 antibodies, after two weeks of the dynamic culture. It has been known that CD31 and CD144 play significant roles in the adhesion during angiogenesis, the control of EC contacts, proliferation, and growth factor reception [57-59]. After two weeks, it was apparent that the engagements of the biomarkers to ECs were significantly promoted over time in the three different groups, as shown in Fig. 8. However, the bifurcation point in the YS group (the presence of the junction with a steep angle) exhibited a relatively weaker engagement than the other areas and groups due to the low spatially alternating shear stress-induced cell retraction [52]. Along with the CFD simulation data, the lack of biomarker engagement and a low volumetric flow rate and WSS could explain the following: 1) Disturbed flow occurring in curvature and bifurcated regions affects the adhesion and microfilament arrangement changes of the ECs and endothelial permeability. 2) The bifurcated regions support less vascular maturation than the unidirectional laminar WSS in an ST vessel, which helps explain the localized occurrence of vascular diseases in these regions of the human body, such as vein thrombosis. Generally, our results demonstrate that the region of flow disturbances near bifurcations results in complex flow and spatiotemporally-varying shear stresses, and the variation of shear stress can regulate the vascular remodeling process, which would contribute to the pathobiology of vascular diseases and predict their susceptibility [60,61].

4. Conclusion

In this study, two 3D printed PLA filaments with polar opposite crystallinities were used to study their physical properties and biological activities in 3D printing artificial small-diameter BV implants for clinical use. Compared to high crystalline PLA, low crystalline PLA exhibited a superior mechanical tolerance with gradual biodegradation and favorite adhesion and growth of ECs. Then three fundamental luminal

geometries of BV implants were 3D printed using LC PLA and cultured in a physiologically-relevant dynamic flow condition. Our results demonstrated that the presence of the dynamic flows was beneficial for the formation of endothelium with an aligned EC arrangement. Moreover, the results of immunostaining and computational modeling illustrated that the geometry-induced flows in the BVs significantly affected cellular behaviors, including cell adhesion, maturation, and function, which is crucial for exploring the pathobiology of vascular diseases. Our study employs 3D printed small-diameter PLA BV implants not only to explore the crystallinity-dependent material characteristics for optimal BV manufacturing, but also to improve our fundamental understanding of geometry-induced BV intimal mechanotransduction.

CRediT authorship contribution statement

Sung Yun Hann: Conceptualization, Methodology, Validation, Formal analysis, Investigation, Data curation, Visualization, Writing – original draft. Haitao Cui: Conceptualization, Methodology, Formal analysis, Validation, Writing – review & editing. Nora Caroline Zalud: Software, Data curation, Visualization, Writing – original draft. Timothy Esworthy: Writing – review & editing. Kartik Bulusu: Methodology, Validation. Yin-Lin Shen: Writing – review & editing. Michael W. Plesniak: Resources, Supervision, Funding acquisition, Writing – review & editing. Lijie Grace Zhang: Project administration, Resources, Supervision, Funding acquisition, Writing – review & editing.

Declaration of competing interest

The authors have no other relevant affiliations or financial involvement with any organization entity with a financial interest in or financial conflict with the subject matter or materials discussed in the manuscript apart from those disclosed.

Acknowledgements

This work is supported by NSF Biomechanics and Mechanobiology Program Award Number 1854415 and American Heart Association Transformative Project Award. The authors also thank the George Washington University Center for Microscopy and Image Analysis and the George Washington University Center for Biomimetics and Bioinspired Engineering.

References

- [1] R. Langer, J.P. Vacanti, Tissue engineering, Science 260 (5110) (1993) 920-926.
- [2] S.S. Virani, A. Alonso, H.J. Aparicio, E.J. Benjamin, M.S. Bittencourt, C. W. Callaway, et al., Heart disease and stroke statistics—2021 update: a report from the American Heart Association, Circulation 143 (8) (2021) e254–e743.
- [3] C.K. Zarins, D.P. Giddens, B. Bharadvaj, V.S. Sottiurai, R.F. Mabon, S. Glagov, Carotid bifurcation atherosclerosis. Quantitative correlation of plaque localization with flow velocity profiles and wall shear stress, Circ. Res. 53 (4) (1983) 502–514.
- [4] G.D. Giannoglou, A.P. Antoniadis, K.C. Koskinas, Y.S. Chatzizisis, Flow and atherosclerosis in coronary bifurcations, EuroIntervention 6 (Suppl J) (2010) J16–J23.
- [5] J. Martorell, P. Santoma, K. Kolandaivelu, V.B. Kolachalama, P. Melgar-Lesmes, J. J. Molins, et al., Extent of flow recirculation governs expression of atherosclerotic and thrombotic biomarkers in arterial bifurcations, Cardiovasc. Res. 103 (1) (2014) 37-46
- [6] J.G. Nemeno-Guanzon, S. Lee, J.R. Berg, Y.H. Jo, J.E. Yeo, B.M. Nam, et al., Trends in tissue engineering for blood yessels. J. Biomed. Biotechnol. 2012 (2012).
- [7] S.Y. Hann, H. Cui, T. Esworthy, S. Miao, X. Zhou, S.-j. Lee, et al., Recent advances in 3D printing: vascular network for tissue and organ regeneration, Transl. Res. 211 (2019) 46–63.
- [8] H. Cui, M. Nowicki, J.P. Fisher, L.G. Zhang, 3D bioprinting for organ regeneration, Adv. Healthc. Mater. 6 (1) (2017) 1601118.
- [9] E.C. Novosel, C. Kleinhans, P.J. Kluger, Vascularization is the key challenge in tissue engineering, Adv. Drug Deliv. Rev. 63 (4–5) (2011) 300–311.
- [10] X. Zhao, L. Liu, J. Wang, Y. Xu, W. Zhang, G. Khang, et al., In vitro vascularization of a combined system based on a 3D printing technique, J. Tissue Eng. Regen. Med. 10 (10) (2016) 833–842.
- [11] Ha TLB, T.M. Quan, D.N. Vu, Naturally derived biomaterials: preparation and application, in: Regenerative Medicine and Tissue Engineering, IntechOpen, 2013.
- [12] S. Pashneh-Tala, S. MacNeil, F. Claeyssens, The tissue-engineered vascular graft—past, present, and future, Tissue Eng. B Rev. 22 (1) (2016) 68–100.
- [13] T.M. Do, Y. Yang, A. Deng, Porous bilayer vascular grafts fabricated from electrospinning of the recombinant human collagen (RHC) peptide-based blend, Polymers 13 (22) (2021) 4042.
- [14] C. Dikyol, M. Altunbek, B. Koc, Embedded multimaterial bioprinting platform for biofabrication of biomimetic vascular structures, J. Mater. Res. 1–14 (2021).
- [15] V.V. Alvino, A.C. Thomas, M.T. Ghorbel, F. Rapetto, S.A. Narayan, M. Kilcooley, et al., Reconstruction of the swine pulmonary artery using a graft engineered with syngeneic cardiac pericytes, Front. Bioeng. Biotechnol. 806 (2021).
- [16] N. Yudintceva, Y.A. Nashchekina, M. Shevtsov, V. Karpovich, G. Popov, I. Samusenko, et al., Small-diameter vessels reconstruction using cell tissueengineering graft based on the polycaprolactone, Cell Tissue Biol. 1–10 (2021).
- [17] J.A. Beckman, Diseases of the veins, Circulation 106 (17) (2002) 2170–2172.
- [18] M. Wu, KK, M.P. Thiagarajan, Role of endothelium in thrombosis and hemostasis, Annu. Rev. Med. 47 (1) (1996) 315–331.
- [19] P. Verhamme, M. Hoylaerts, The pivotal role of the endothelium in haemostasis and thrombosis, Acta Clin. Belg. 61 (5) (2006) 213–219.
- [20] P.L. Gross, W.C. Aird (Eds.), The Endothelium and Thrombosis. Seminars in Thrombosis and Hemostasis, Copyright© 2000 by Thieme Medical Publishers, Inc., 333 Seventh Avenue, New, 2000.
- [21] A wireless microsensor for monitoring flow and pressure in a blood vessel utilizing a dual-inductor antenna stent and two pressure sensors, in: K. Takahata, A. DeHennis, K.D. Wise, Y.B. Gianchandani (Eds.), 17th IEEE International Conference on Micro Electro Mechanical Systems Maastricht MEMS 2004 Technical Digest, IEEE, 2004.
- [22] H. Cui, S. Miao, T. Esworthy, X. Zhou, S.-j. Lee, C. Liu, et al., 3D bioprinting for cardiovascular regeneration and pharmacology, Adv. Drug Deliv. Rev. 132 (2018) 252–269.
- [23] S.Y. Hann, H. Cui, T. Esworthy, X. Zhou, S.-j. Lee, M.W. Plesniak, et al., Dual 3D printing for vascularized bone tissue regeneration, Acta Biomater. 123 (2021) 263–274.
- [24] R.R. Jose, M.J. Rodriguez, T.A. Dixon, F. Omenetto, D.L. Kaplan, Evolution of bioinks and additive manufacturing technologies for 3D bioprinting, ACS Biomater. Sci. Eng. 2 (10) (2016) 1662–1678.
- [25] M. Zhang, R. Lin, X. Wang, J. Xue, C. Deng, C. Feng, et al., 3D printing of Haversian bone–mimicking scaffolds for multicellular delivery in bone regeneration, Sci. Adv. 6 (12) (2020), eaaz6725.
- [26] B.S. Kim, Y.W. Kwon, J.-S. Kong, G.T. Park, G. Gao, W. Han, et al., 3D cell printing of in vitro stabilized skin model and in vivo pre-vascularized skin patch using tissue-specific extracellular matrix bioink: a step towards advanced skin tissue engineering, Biomaterials 168 (2018) 38–53.
- [27] S. Michael, H. Sorg, C.-T. Peck, L. Koch, A. Deiwick, B. Chichkov, et al., Tissue engineered skin substitutes created by laser-assisted bioprinting form skin-like structures in the dorsal skin fold chamber in mice, PLoS One 8 (3) (2013), e57741.
- [28] S.-j. Lee, D. Yan, X. Zhou, H. Cui, T. Esworthy, S.Y. Hann, et al., Integrating cold atmospheric plasma with 3D printed bioactive nanocomposite scaffold for cartilage regeneration, Materials Science and Engineering; C 111 (2020) 110844.
- [29] X. Zhou, S. Tenaglio, T. Esworthy, S.Y. Hann, H. Cui, T.J. Webster, et al., Three-dimensional printing biologically inspired DNA-based gradient scaffolds for cartilage tissue regeneration, ACS Appl. Mater. Interfaces 12 (29) (2020) 33219–33228.

- [30] Y.S. Zhang, A. Arneri, S. Bersini, S.-R. Shin, K. Zhu, Z. Goli-Malekabadi, et al., Bioprinting 3D microfibrous scaffolds for engineering endothelialized myocardium and heart-on-a-chip, Biomaterials 110 (2016) 45–59.
- [31] Y. Wang, H. Cui, Y. Wang, C. Xu, T.J. Esworthy, S.Y. Hann, et al., 4D printed cardiac construct with aligned myofibers and adjustable curvature for myocardial regeneration, ACS Appl. Mater. Interfaces 13 (11) (2021) 12746–12758.
- [32] T.N.A.T. Rahim, A.M. Abdullah, Akil H. Md, Recent developments in fused deposition modeling-based 3D printing of polymers and their composites, Polym. Rev. 59 (4) (2019) 589–624.
- [33] T. Agarwal, G.M. Fortunato, S.Y. Hann, B. Ayan, K.Y. Vajanthri, D. Presutti, et al., Recent advances in bioprinting technologies for engineering cardiac tissue, Mater. Sci. Eng. C Mater. Biol. Appl. 124 (2021), 112057.
- [34] M. Guvendiren, J. Molde, R.M. Soares, J. Kohn, Designing biomaterials for 3D printing, ACS Biomater. Sci. Eng. 2 (10) (2016) 1679–1693.
- [35] T. Serra, M.A. Mateos-Timoneda, J.A. Planell, M. Navarro, 3D printed PLA-based scaffolds: a versatile tool in regenerative medicine, Organogenesis 9 (4) (2013) 239–244.
- [36] D. Garlotta, A literature review of poly (lactic acid), J. Polym. Environ. 9 (2) (2001) 63–84.
- [37] B. Wittbrodt, J.M. Pearce, The effects of PLA color on material properties of 3-D printed components, Addit. Manuf. 8 (2015) 110–116.
- [38] J.J. Schwartz, J. Hamel, T. Ekstrom, L. Ndagang, A.J. Boydston, Not all PLA filaments are created equal: an experimental investigation, Rapid Prototyp. J. 26 (7) (2020) 1263–1276.
- [39] V.A. Zhuikov, E.A. Akoulina, D.V. Chesnokova, Y. Wenhao, T.K. Makhina, I. V. Demyanova, et al., The growth of 3T3 fibroblasts on PHB, PLA and PHB/PLA blend films at different stages of their biodegradation in vitro, Polymers 13 (1) (2020).
- [40] F. Kawai, in: Polylactic Acid (PLA)-degrading Microorganisms and PLA Depolymerases 1043, 2010, pp. 405–414.
- [41] S.H. Lee, I.Y. Kim, W.S. Song, Biodegradation of polylactic acid (PLA) fibers using different enzymes, Macromol. Res. 22 (6) (2014) 657–663.
- [42] T.K. Villiger, B. Neunstoecklin, D.J. Karst, E. Lucas, M. Stettler, H. Broly, et al., Experimental and CFD physical characterization of animal cell bioreactors: from micro-to production scale, Biochem. Eng. J. 131 (2018) 84–94.
- [43] M. Tanaka, G. Girard, R. Davis, A. Peuto, N. Bignell, Recommended table for the density of water between 0 C and 40 C based on recent experimental reports, Metrologia 38 (4) (2001) 301.
- [44] L. Korson, W. Drost-Hansen, F.J. Millero, Viscosity of water at various temperatures, J. Phys. Chem. 73 (1) (1969) 34–39.
- [45] U. Klun, J. Friedrich, A. Kržan, Polyamide-6 fibre degradation by a lignolytic fungus, Polym. Degrad. Stab. 79 (1) (2003) 99–104.
- [46] K. Park, M. Xanthos, A study on the degradation of polylactic acid in the presence of phosphonium ionic liquids, Polym. Degrad. Stab. 94 (5) (2009) 834–844.
- [47] D. Jung, Enzymology, Daegwangseolim, Seoul, 2003.
- [48] J. Walsh, Ecological considerations of biodeterioration, Int. Biodeterior. Biodegradation 48 (1–4) (2001) 16–25.
- [49] B.L. Langille, Integrity of arterial endothelium following acute exposure to high shear stress, Biorheology 21 (3) (1984) 333–346.
- [50] B.D. Johnson, K.J. Mather, J.P. Wallace, Mechanotransduction of shear in the endothelium: basic studies and clinical implications, Vasc. Med. 16 (5) (2011) 365–377.
- [51] M. Klarhöfer, B. Csapo, C. Balassy, J. Szeles, E. Moser, High-resolution blood flow velocity measurements in the human finger, Magn. Reson. Med. 45 (4) (2001) 716–719
- [52] P.F. Davies, A. Remuzzi, E.J. Gordon, C.F. Dewey, M.A. Gimbrone, Turbulent fluid shear stress induces vascular endothelial cell turnover in vitro, Proc. Natl. Acad. Sci. 83 (7) (1986) 2114–2117.
- [53] P.F. Davies, Hemodynamic shear stress and the endothelium in cardiovascular pathophysiology, Nat. Clin. Pract. Cardiovasc. Med. 6 (1) (2009) 16–26.
- [54] M.A. Gimbrone Jr., G. García-Cardeña, Endothelial cell dysfunction and the pathobiology of atherosclerosis, Circ. Res. 118 (4) (2016) 620–636.
- [55] J. Siggers, S. Waters, Steady flows in pipes with finite curvature, Phys. Fluids 17 (7) (2005), 077102.
- [56] C. Cox, M.R. Najjari, M.W. Plesniak, Three-dimensional vortical structures and wall shear stress in a curved artery model, Phys. Fluids 31 (12) (2019), 121903.
- [57] X. Zhou, M. Nowicki, H. Sun, S.Y. Hann, H. Cui, T. Esworthy, et al., 3D bioprinting-tunable small-diameter blood vessels with biomimetic biphasic cell layers, ACS Appl. Mater. Interfaces 12 (41) (2020) 45904–45915.
- [58] D. Vestweber, VE-cadherin: the major endothelial adhesion molecule controlling cellular junctions and blood vessel formation, Arterioscler. Thromb. Vasc. Biol. 28 (2) (2008) 223–232.
- [59] M.P. Pusztaszeri, W. Seelentag, F.T. Bosman, Immunohistochemical expression of endothelial markers CD31, CD34, von Willebrand factor, and Fli-1 in normal human tissues, J. Histochem. Cytochem. 54 (4) (2006) 385–395.
- [60] Y.-S.J. Li, J.H. Haga, S. Chien, Molecular basis of the effects of shear stress on vascular endothelial cells, J. Biomech. 38 (10) (2005) 1949–1971.
- [61] J.-J. Chiu, S. Chien, Effects of disturbed flow on vascular endothelium: pathophysiological basis and clinical perspectives, Physiol. Rev. 91 (1) (2011) 327–387.